Journal of ELECTRONIC MATERIALS, Vol. 49, No. 2, 2020
https://doi.org/10.1007/s11664-019-07841-z

Ternary $CuCo_2S_4$ Thiospinel Nanocrystal-Coated Photodiode with Improved Photoresponsivity and Acceptance Angles for Optoelectronic Applications

MURAT YILDIRIM,[1,6] ADEM KOCYIGIT,[2] ADEM SARILMAZ,[3] SULTAN SULEYMAN OZEL,[3] MAHMUT KUS,[4] and FARUK OZEL[3,5,7]

1.—Department of Biotechnology, Faculty of Science, Selcuk University, 42130 Konya, Turkey. 2.—Department of Electrical Electronics Engineering, Engineering Faculty, Igdir University, 76000 Igdir, Turkey. 3.—Department of Metallurgical and Materials Engineering, Faculty of Engineering, Karamanoglu Mehmetbey University, 70200 Karaman, Turkey. 4.—Department of Chemical Engineering, Faculty of Engineering and Natural Sciences, Konya Technical University, 42075 Konya, Turkey. 5.—Scientific and Technological Research and Application Center, Karamanoglu Mehmetbey University, 70200 Karaman, Turkey. 6.—e-mail: muratyildirim@selcuk.edu.tr. 7.—e-mail: farukozell@gmail.com

Ternary-structured thiospinels have attracted great attention in recent years for energy applications due to their attractive characteristics such as simple production, earth-abundant components and non-toxic nature. In this work, copper cobalt sulfide ($CuCo_2S_4$ or carrollite) thiospinel nanocrystals were synthesized by a hot-injection method, and detailed electrical and optoelectronic characterizations were performed in a Schottky device. The synthesized nanocrystals were used as an interfacial layer between the Au metal and *p*-Si semiconductor to obtain an Au/$CuCo_2S_4$/*p*-Si device. The structural and morphological characterizations confirmed the crystallinity, nanostructure and composition of the $CuCo_2S_4$ nanocrystals. The *I*–*V* and *C*–*V* measurements were employed to characterize the Au/$CuCo_2S_4$/*p*-Si device for various illumination intensities. The obtained device exhibited good rectifying and photodiode properties as well as good photocapacitance. The Au/$CuCo_2S_4$/*p*-Si device can be used and improved for optoelectronic applications.

Key words: $CuCo_2S_4$, carrollite, photodiode, optoelectronic properties, hot-injection method

INTRODUCTION

Energy demand is a very important indication of development of societies in terms of its consumption and efficient management. Developed countries want to use renewable energies instead of fossil fuels, which are limited and harmful for the environment. Efficient renewable energy conversion generally requires expensive materials such as Au and Pt. There is much demand for the synthesis of alternative materials instead of expensive raw materials for renewable energy. As a result, $CuCo_2S_4$ has been developed for energy applications, but there are only a few studies in the literature on the synthesis and application of these materials.[1–3] For example, Chauhan et al.[2] synthesized $CuCo_2S_4$ nanosheets by a hydrothermal method and used the produced materials in a hydrogen production application. Similarly, $CoNi_2S_4$ and $CuCo_2S_4$ were obtained with a solvothermal technique by Ge et al.[4] for use in hydrogen production. In another study, $CuCo_2S_4$ nanosheets were synthesized by a hydrothermal method and employed as catalyst in an oxygen evolution reaction.[5] In parallel with this study, the electrocatalytic properties of this material were produced by a solution-based chemical route and

(Received September 17, 2019; accepted November 15, 2019; published online November 27, 2019)

investigated for an oxygen evolution reaction.[6] According to a study of Du et al.,[7] flower-like $CuCo_2S_4$ was synthesized in microsphere shapes via a hydrothermal method, and water oxidation activity stability during water oxidation of the produced materials was examined. Chen et al.[8] reported that $CuCo_2S_4$ nanosheets were synthesized by a solvothermal route and employed in supercapacitor applications. Similar to the previous study, mesostructure particles were used in an asymmetric supercapacitor application, but these materials were produced as $CuCo_2S_4/CuCo_2O_4$ heterostructures by a solvothermal method.[9] Cheng et al.[10] studied the synthesis of porous $CuCo_2S_4$ by a two-step hydrothermal technique and investigated the use of the obtained nanorod arrays in an asymmetric supercapacitor application. $CuCo_2S_4$ sub-microsphere particles were employed in lithium/sodium-ion batteries, which is one of the different application areas, and sub-microspheres were synthesized by a one-pot solvothermal method.[11] Li et al.[12] synthesized hydrophilic $CuCo_2S_4$ nanocrystals by a hydrothermal method and used them in magnetic resonance/near-infrared imaging. Chen et al.[13] synthesized yolk-shell-shaped $CuCo_2S_4$ materials by anion exchange and employed them for photocatalytic degradation of methylene blue dye. They concluded that the photocatalytic performance of the $CuCo_2S_4$ materials increased via new geometric structure. However, while certain applications of $CuCo_2S_4$ have been studied, to our best knowledge, no studies in the literature have investigated the photodiode properties of $CuCo_2S_4$ nanocrystals.

Therefore, this study provides an important contribution to the detailed characterization studies of $CuCo_2S_4$, which is one of the thiospinel materials most widely used in the literature. Here, we have successfully synthesized $CuCo_2S_4$ nanocrystals by a facile hot-injection technique. The structural characterization results showed that the synthesized materials have the desired crystal structure, 8 nm in size and homogeneous atomic distribution. The as-synthesized nanocrystals were employed as an interfacial layer between the Au metal contact and *p*-Si semiconductor. The obtained device was characterized by *I–V* and *C–V* measurements under dark and various illumination conditions.

EXPERIMENTAL DETAILS

Cobalt (II) acetate ($Co(CO_2CH_3)_2$, 99.995%), copper (II) acetate ($Cu(CO_2CH_3)_2$, 99.99%), ethanol (99.9%), trioctylphosphine oxide ((TOPO) (99%)), 1-dodecanethiol (DDT, 98%), tert-dodecanethiol (t-DDT, 98%), and 1-octadecene (ODE, 90% tech) were purchased from Sigma-Aldrich. Toluene (99%) was obtained from the VWR International Company. All chemicals were used without any further purification.

$CuCo_2S_4$ thiospinel nanocrystals were synthesized following a method reported by Sarilmaz et al.,[14] with minor modifications. Briefly, 45 mg of $Cu(CO_2CH_3)_2$, 88 mg of $(CH_3CO_2)_2Co$, 1.75 mmol TOPO and 10 mL ODE were loaded into a 50 mL two-necked flask and heated to 210°C with magnetic stirring under argon flow. Freshly prepared sulfur solution (0.875 mL (t-DDT) and 0.125 mL (DDT)) was then rapidly injected (≈ 120°C) into the hot reaction mixture under vigorous stirring. Under these conditions, the reaction was continued for 30 min, and the mixture was then cooled to room temperature. Finally, the reaction medium was cooled to 80°C, and a toluene–ethanol mixture was added. After that, they were separated by centrifugation at a rate of 4000 r/min for 1 min. Although the interface is different, the methods of the heterojunction device are the same as in our previous studies.[15,16] The resulting structure was obtained as $Au/CuCo_2S_4/p$-Si. Here, a (100)-oriented *p*-type Si wafer with 7.15×10^{15} cm^3 carrier concentration was sliced to 1.5 cm^2 pieces and used as substrate and semiconductor material. While the 100 nm thicknesses Al layer was evaporated to the back surface of the substrate for ohmic contact, a 100 nm Au layer was vaporized on the $CuCo_2S_4$ films as rectifying contact. The ohmic contact was annealed in an N_2 atmosphere at 500°C for 5 min after evaporation of the Al contact. Figure 1a and b shows schematically the obtained $Au/CuCo_2S_4/p$-Si device and its band diagram, respectively. According to the band diagram, the device has a barrier height and an interfacial layer between the Au and *p*-Si. This interfacial layer may be the cause of the increased barrier height between the Au and *p*-Si.

X-ray diffractometer (XRD) measurements were obtained by a Bruker D8 x-ray diffractometer with Cu-Kα radiation at 0.15418 nm wavelength. An FEI brand TALOS F200S model tunneling electron microscope (TEM) was used to take images of the $CuCo_2S_4$ nanocrystals by 200 kV acceleration. Fast mapping and composition of the $CuCo_2S_4$ nanocrystals were obtained by Hitachi SU5000 model scanning electron microscope—energy dispersive x-ray spectroscopy (SEM–EDX) instruments. The *I–V* data were collected by a Fytronix FY-5000, and *C–V* measurements were obtained by a Keithley 4200 SCS under dark and various illumination conditions per cm^2 device area.

RESULTS AND DISCUSSION

Figure 2a shows the XRD pattern of the synthesized $CuCo_2S_4$ nanocrystals. The main pronounced peaks at 2θ = 26.5°, 31.3°, 38°, 46.9°, 50° and 54.75° respectively correspond to the (022), (113), (004), (224), (115) and (044) planes of the $CuCo_2S_4$ structure. All the diffraction peaks can be indexed to cubic-$CuCo_2S_4$ (JSPDS No. 042-1450), and no other peaks of impurity phase were detected. Debye–Scherrer analysis of the peak broadening of all main peaks revealed crystallite dimensions of around 8.5 nm.[17] The average elemental composition ratio

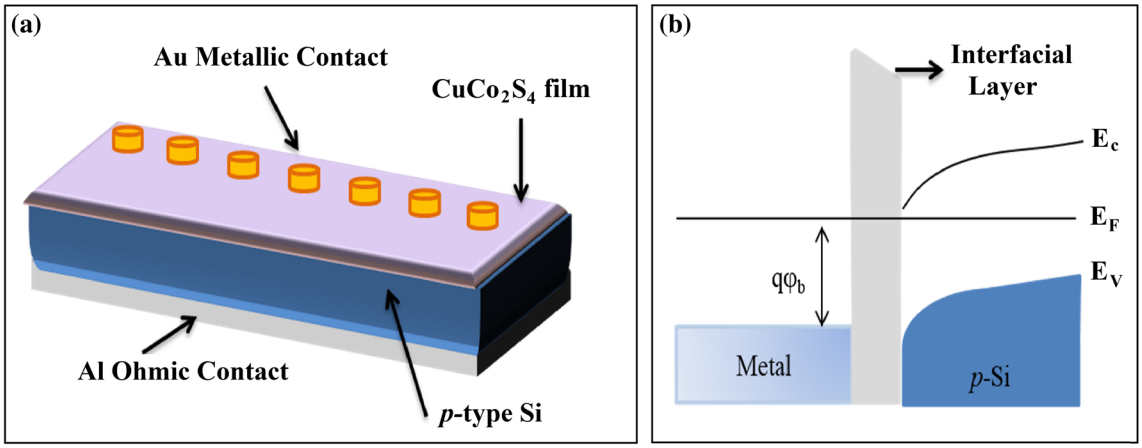

Fig. 1. (a) Schematic illustration and (b) band diagram of the Au/$CuCo_2S_4$/*p*-Si device.

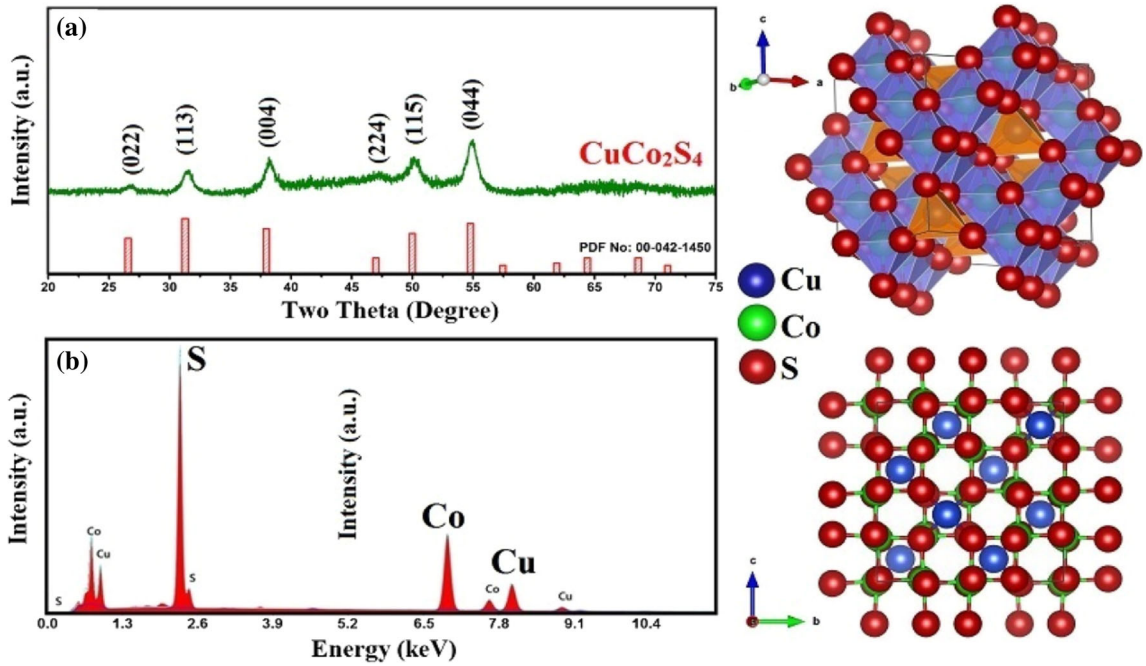

Fig. 2. (a) XRD pattern (b) EDS spectrum, and corresponding crystal structure of the $CuCo_2S_4$ nanocrystals is shown on the right side.

of the $CuCo_2S_4$ nanocrystals was analyzed by EDS. The EDS result is shown in Fig. 2b. The EDS spectrum of the $CuCo_2S_4$ nanocrystals shows the significant presence of only copper, cobalt and sulfur, with an atomic ratio (Cu/Co/S) of nearly 1:2:4, in good agreement with the stoichiometric molar ratio of carrollite.

Figure 3a and b shows typical TEM images of synthesized $CuCo_2S_4$ nanocrystals. As can be seen in Fig. 3b, the $CuCo_2S_4$ nanocrystals display a nearly spherical shape, and the average size was measured as 8 $\pm$ 0.5 nm, in good agreement with the calculated crystal structure from XRD measurements by the Debye–Scherrer equation. Figure 3e represents the FE-SEM images of the nanocrystals. As shown in Fig. 3e, the nanocrystals exhibit an agglomerated morphology. These results are consistent with the TEM results and can be observed in general nanoparticles. In addition, we used HR-TEM to further confirm the crystallinity and structure of the $CuCo_2S_4$ nanocrystals. According to high-resolution TEM (HR-TEM) images (Fig. 3c), lattice fringes with interplanar spacing of 2.37 Å. ((044) crystallographic planes)), corresponding to a high degree of structural ordering for these $CuCo_2S_4$, are clearly seen, which implies a fully crystalline structure. The well-resolved fringes confirm the local crystallinity of the $CuCo_2S_4$ nanocrystals, which is in good harmony by selected area electron diffraction (SAED) pattern, and it is shown in Fig. 3d. In Fig. 3d, all diffraction rings are discontinuous and consist of sharp spots, which

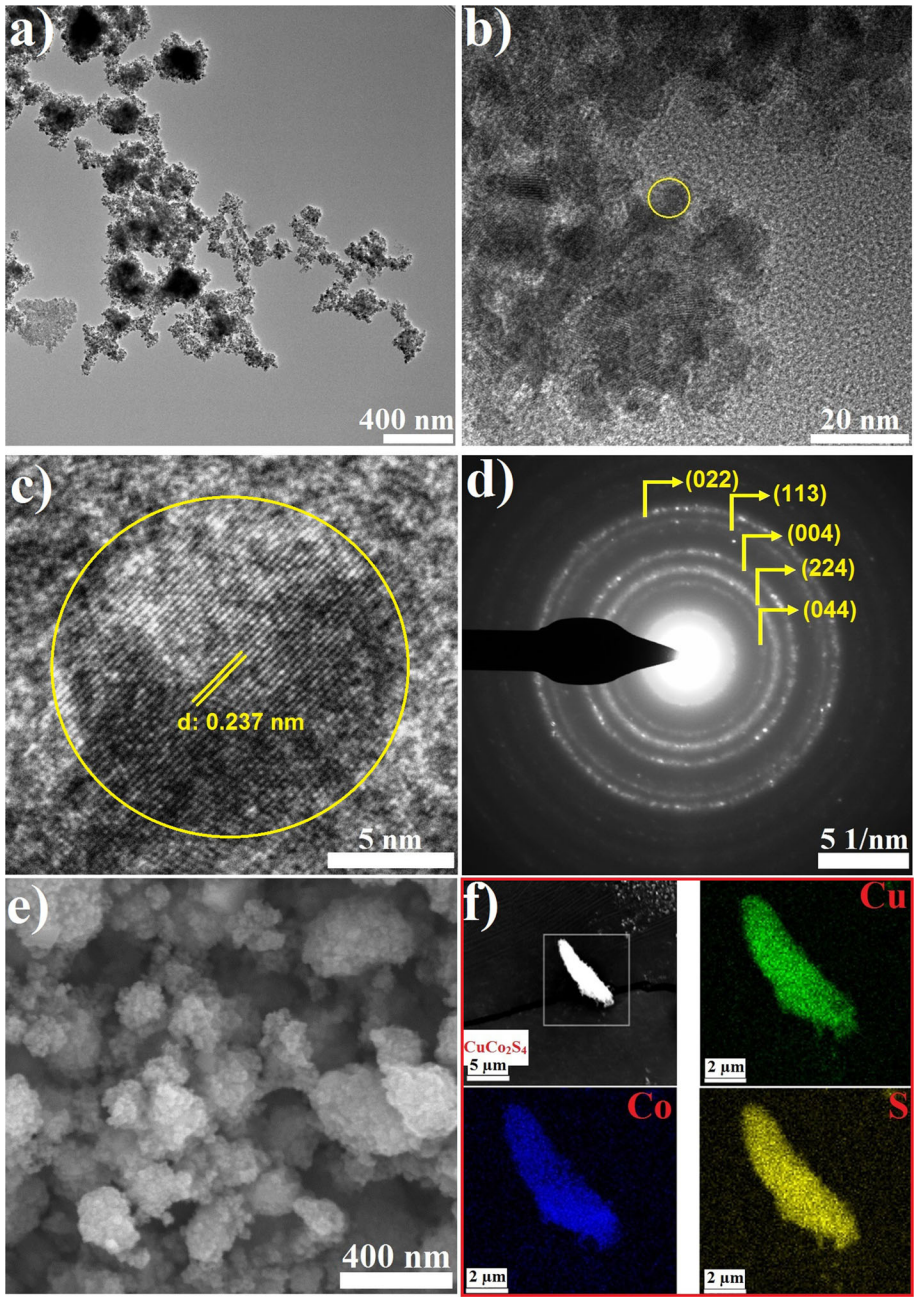

Fig. 3. (a, b) TEM, (c) HR-TEM, (d) SAED, (e) SEM and (f) SEM-elemental mapping images of the $CuCo_2S_4$ nanocrystals.

indicate that the nanocrystals are well crystallized.[18] Figure 3f displays the elemental mapping images for the $CuCo_2S_4$ structures. The EDS images clearly show that the sample contains copper, cobalt and sulfur atoms, and these atoms are homogeneously distributed for all of the samples. These results clearly emphasize that homogeneous $CuCo_2S_4$ structures can be successfully synthesized by the hot-injection method.

I–V plot of the Au/$CuCo_2S_4$/*p*-Si device is shown in Fig. 4 under dark and various illumination conditions in the range of 20–100 mW by 20 mW intervals per cm^2 device area. The Au/$CuCo_2S_4$/*p*-Si device exhibited a good rectifying property and the rectifying ratio of the device was obtained as 8.28×10^3 at 5 V. Furthermore, the Au/$CuCo_2S_4$/*p*-Si device has a photodiode property at reverse biases because the current of the device increased by increasing light illumination intensity from 2.28×10^{-7} A at dark to 5.89×10^{-5} A 100 mW light illumination intensities. The photodiode property of the Au/$CuCo_2S_4$/*p*-Si device is based on the increasing carriers in the interface of the metal–semiconductor junction by light intensity.[19] Normally, $CuCo_2S_4$ has a 1.41 eV band gap and can easily absorb the solar spectrum.[13] In this case, the

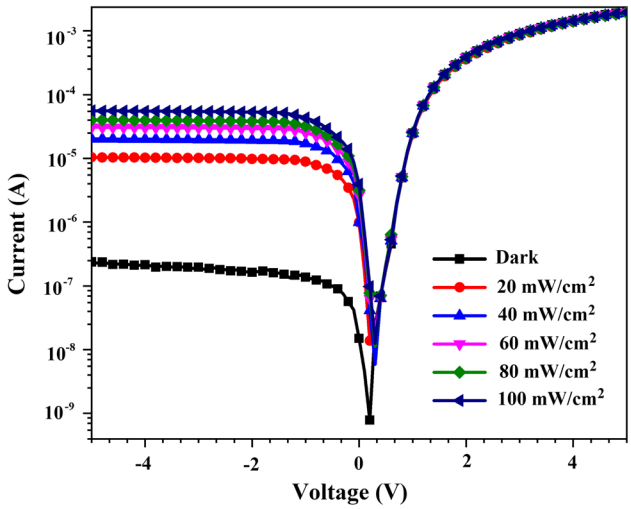

Fig. 4. In *I–V* plots of the Au/$CuCo_2S_4$/*p*-Si device under dark and various illuminations for per cm^2 device area.

$CuCo_2S_4$ may cause a barrier between the Al and *p*-Si and decrease the current amount at reverse biases. However, the obtained Au/$CuCo_2S_4$/*p*-Si device can be employed by improving its photodiode property with homogeneous interfacial layers.[20,21]

Diode parameters (barrier height (Φ_b), ideality factor (n) and series resistance (R_s)) are determined to understand the device property better. There are three most popular techniques to calculate diode parameters. One of these techniques is thermionic emission theory and can help to obtain the ideality factor and barrier height by *I–V* measurements data. This technique describes the current (I) as the following formula:

$$I = I_0 \exp\left(\frac{qV}{nkT}\right)\left[1 - \exp\left(-\frac{qV}{nkT}\right)\right], \quad (1)$$

where I_0 represents saturation current. q, k and V are the charge of electron, Boltzmann's constant and the applied bias voltage, respectively. The I_0 is given via the following equation:

$$I_0 = AA^*T^2 \exp\left(-\frac{q\Phi_b}{kT}\right), \quad (2)$$

where A, A^* and T are diode area (A =7.85 × 10^{-3} cm^2), Richardson constant and the temperature, respectively. The n and Φ_b are calculated via the following equations for $V \geq 3kT/q$.

$$n = \frac{q}{kT}\left(\frac{dV}{d\ln I}\right) \quad (3)$$

and

$$\Phi_b = \frac{kT}{q}\ln\left(\frac{A^*AT^2}{I_0}\right). \quad (4)$$

The I_0 was determined as 1.12 × 10^{-9} A for the Au/$CuCo_2S_4$/*p*-Si device from the ln *I–V* plot for a second linear region in between 0.25 V and 0.98 V, and thus the Φ_b value was calculated. The n and Φ_b values were calculated as 3.63 eV and 0.79 eV, respectively. Normally, an ideal metal–semiconductor device has 1.0 n value, but a non-ideal device is usually a bigger n value than one depending on various reasons such as barrier inhomogeneity,[22] series resistance effect,[23] interface states[24] and non-uniform distribution of interfacial charges.[25] The bigger n value than one for Au/$CuCo_2S_4$/*p*-Si device can be attributed to barrier inhomogeneity and non-uniform $CuCo_2S_4$ interfacial layer.[26,27] Furthermore, the Au/$CuCo_2S_4$/*p*-Si device maintained rectifying property at 100 mW light intensities as 3.46 × 10^1. This result confirmed that $CuCo_2S_4$ material can be employed as photodiode and photodetector applications. The obtained barrier height values were calculated as 0.79 eV. This Φ_b value is higher than the Au/*p*-Si device depending on interfacial layer effect of the $CuCo_2S_4$ layer according to the literature.[28,29]

To determine the series resistance effect on the device, Cheung's technique should be performed for the Au/$CuCo_2S_4$/*p*-Si device. This technique provides calculation of barrier height and ideality factor values as well as series resistance (R_s) by *I–V* measurements.[30]

Cheung approximation gives the current as in the following formula:

$$I = I_0 \exp\left(\frac{q(V - IR_s)}{nkT}\right), \quad (5)$$

where the IR_s term indicates voltage drop depending on series resistance of a junction. The formula can be rearranged for R_s and Cheung's functions are obtained as in the following equations:

$$\frac{dV}{d(\ln I)} = IR_s + n\frac{kT}{q}, \quad (6)$$

$$H(I) = V - n\left(\frac{kT}{q}\right)\ln\left(\frac{I}{AA^*T^2}\right), \quad (7)$$

where $H(I)$ can be typed as:

$$H(I) = IR_s + n\Phi_b. \quad (8)$$

Plotting of $dV/d(\ln I)$ versus I provides determining the ideality factor and one of the series resistance values, and $H(I)$ versus I graph gives barrier height and another series resistance. The details about calculation via Cheung technique can be find in the literature.[31–33] Two R_s values are used for proof of the consistency for Cheung's functions.[34]

Figure 5 displays $dV/d(\ln I)$ versus I and $H(I)$ versus I graphs of the Au/$CuCo_2S_4$/*p*-Si device via exhibiting good linearity. The obtained n and Φ_b values are 3.56 eV and 0.81 eV, respectively. The series resistance values were determined as 1.98 kΩ for $dV/d(\ln I)$–I plot and 1.99 kΩ for $H(I)$–I. The determined R_s values are in good harmony with

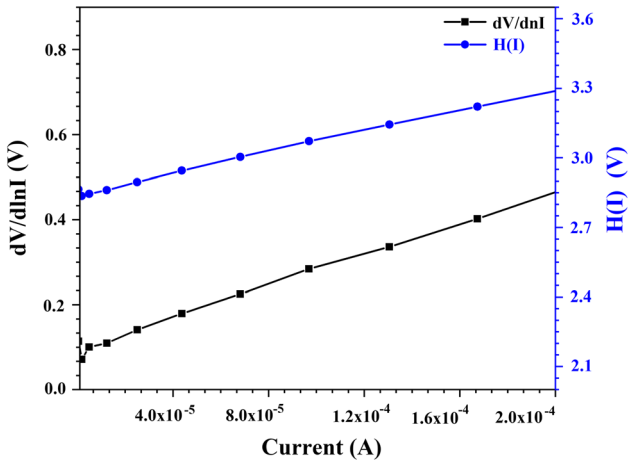

Fig. 5. dV/d(ln$I$)–I and $H(I)$–I graphs of the Au/$CuCo_2S_4$/p-Si device.

each other and confirmed the consistency of the Cheung technique. However, there are slightly differences for n and Φ_b values between Cheung and thermionic emission theory depending on approximation differences.[35]

Another commonly used technique to determine barrier height and series resistance is the Norde method. According to this technique, the Norde function is given in the following equation[16,36]:

$$F(V) = \frac{V}{\gamma} - \frac{kT}{q}\ln\left(\frac{I(V)}{AA^*T^2}\right), \tag{9}$$

where γ is the closest integer higher than the thermionic emission n value. The $I(V)$ represents the voltage-dependent current. If the Norde function is rearranged for the Φ_b and R_s, the following equations are obtained:

$$\Phi_b = F(V_0) + \left[\frac{V_0}{\gamma} - \frac{kT}{q}\right], \tag{10}$$

$$R_s = \frac{\gamma - n}{I}\frac{kT}{q}, \tag{11}$$

where V_0 indicates minimum voltage value depending to $F(V)$.

$F(V)$–V graphs of the Au/$CuCo_2S_4$/p-Si device are shown in Fig. 6. The Φ_b and R_s values were calculated as 0.93 eV and 1.95 kΩ, respectively from the Norde technique. The obtained R_s value is in good agreement with Cheung's R_s values, but there is a difference for obtained Φ_b values between Norde and other techniques. This differences can be based to non-ideal diode structure and barrier inhomogeneity of the device.[15]

The current transient measurements for light-on and light-off conditions show response to the light of an optoelectronic device.[37] The current transient plots of the Au/$CuCo_2S_4$/p-Si device have been shown in Fig. 7 for various illumination intensities. Photocurrent and photoresponse sensitivity speed of

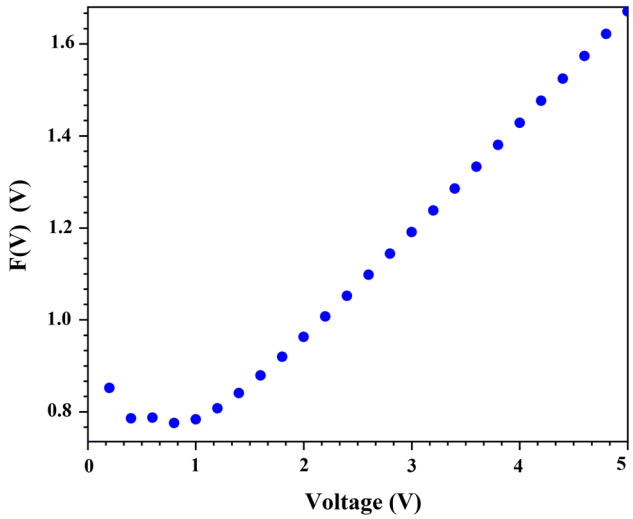

Fig. 6. $F(V)$–V graph of the Au/$CuCo_2S_4$/p-Si device.

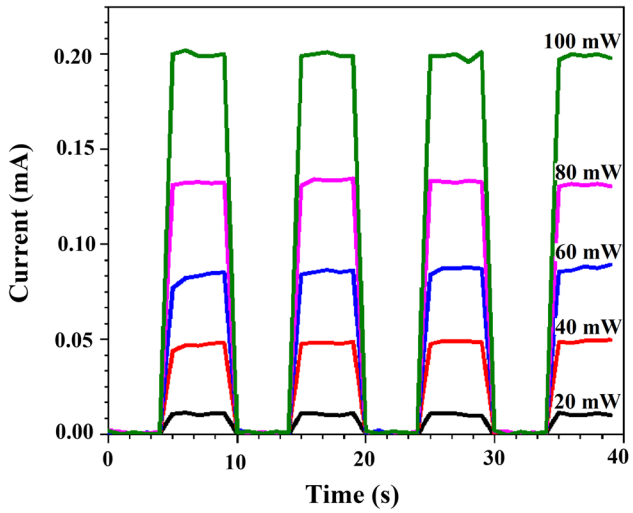

Fig. 7. The current transient measurements of the Au/$CuCo_2S_4$/p-Si device per cm^2 device area.

the Au/$CuCo_2S_4$/p-Si device increased linearly with increasing light intensity. The Au/$CuCo_2S_4$/p-Si device can be used as a photodetector for the detection of light intensity.

Figure 8 indicates the C–V graphs of the Au/$CuCo_2S_4$/p-Si device for a wide range frequency from 10 kHz to 1 MHz. The capacitance values exhibited peaks at the inversion region and remained constant at the accumulation region via changing frequency and voltage. While the peak intensity increased with decreasing frequency, the peak positions usually shifted towards the depletion region. The peaks demonstrated at the inversion region can be attributed to series resistance and interface states.[38,39] The decreasing peak intensity via increasing frequency is related to the fact that interface states cannot follow ac signal at higher frequencies.[40] Even if 1 MHz frequency value was applied on the device, the device still exhibited

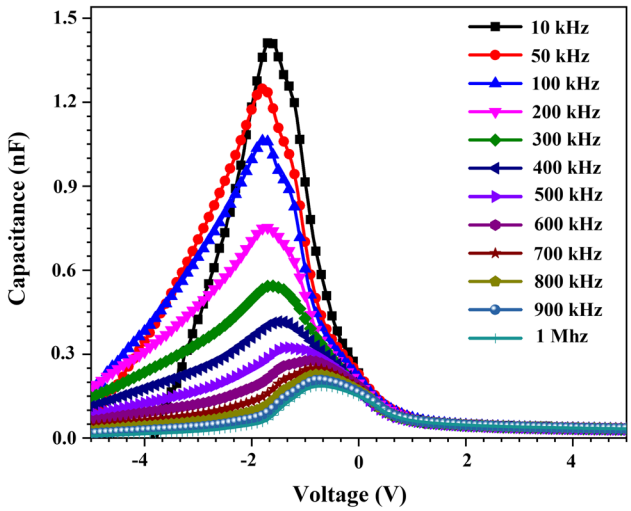

Fig. 8. The capacitance–voltage (C–V) characteristics of the Au/$CuCo_2S_4$/p-Si device.

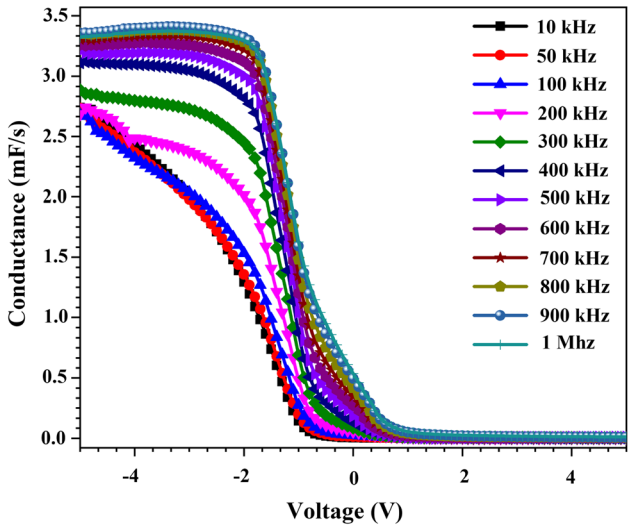

Fig. 9. The conductance–voltage (G–V) characteristics of the Au/$CuCo_2S_4$/p-Si device.

peaks in the depletion region. The peaks at higher frequency may be dependent on the interfacial $CuCo_2S_4$ layer.

The G–V plots of the Au/$CuCo_2S_4$/p-Si device are shown in Fig. 9 for various frequencies. Conductance values decreased linearly in the inversion region for 10 kHz, 50 kHz and 100 kHz frequencies, but plateaued and then suddenly decreased at higher frequencies towards the depletion region. They remained constant at the accumulation region via changing frequency and voltage. The increasing conductance values via increasing frequency at the inversion region can be attributed to a series resistance effect on interface states of the device.[41] The series resistance effect on the device prevents correct capacitance and conductance values and is usually corrected for that reason.[42]

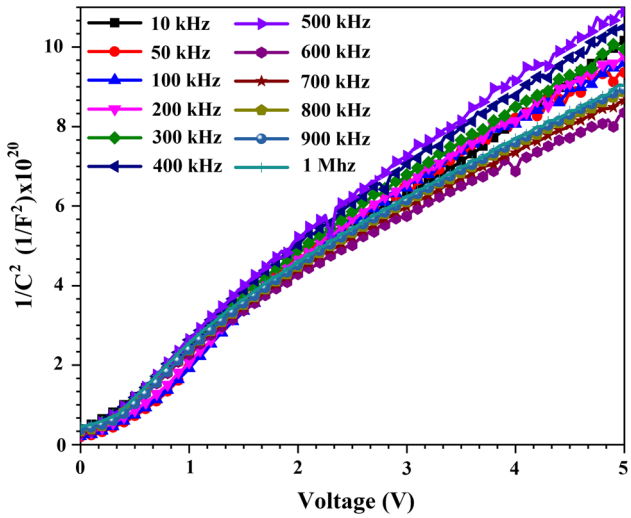

Fig. 10. The C^{-2}–V characteristics of the Au/$CuCo_2S_4$/p-Si device.

Figure 10 indicates C^{-2}–V graphs of the Au/$CuCo_2S_4$/p-Si device for the 10 kHz–1 MHz frequency range. The C^{-2}–V graphs exhibit almost straight lines for a wide range of voltages. The small deviation from linearity can be attributed to the interfacial $CuCo_2S_4$ layer between the Au metal contact and p-Si substrate.[43] The C^{-2}– graphs for metal–semiconductor devices can be used to calculate electrical parameters such as doping concentration of acceptor atoms (N_a), Fermi-level (E_F), barrier height, width of depletion layer (W_d) and maximum electric field (E_m). The electrical parameters were calculated and are given in Table I for various frequencies.[44]

The interface state (N_a) values have fluctuation behavior between 1.100×10^{15} and 1.469×10^{15} cm^{-3} for various frequencies. The Φ_b values also exhibited fluctuations between the 0.866 eV and 1.610 eV values for various frequencies. While the lowest Φ_b value was obtained for 10 kHz, the highest Φ_b value was calculated for the 600 kHz frequency. The E_F values did not change via changing frequency. Both E_m and W_d have variations for various frequencies, but the lowest values of E_m and W_d were obtained for 10 kHz frequency and the highest values were calculated for 1 MHz frequency.

The C–V measurements can help to calculate interface states and series resistance. Those parameters are important for the effects of electrical properties. The N_{ss} and R_s parameters are calculated depending on frequency by the Hill-Coleman method. According to this technique, the N_{ss} is calculated via the following formula[45]:

$$N_{ss} = \frac{2}{qA} \frac{(G_m/\omega)_{max}}{((G_m/\omega)_{max}/C_{0x})^2 + (1 - C_m/C_{0x})^2}, \quad (12)$$

where ω and A are angular frequency and contact area of the device, respectively. The C_m and G_m show measured capacitance and conductance. The

Table I. Some electrical parameters of the Au/$CuCo_2S_4$/*p*-Si device for various frequencies

f (kHz)	N_a ($\times 10^{15}$ cm^{-3})	R_s (Ω)	Φ_b (eV)	E_F (eV)	E_m ($\times 10^4$ V/cm)	W_d ($\times 10^{-4}$ cm)	N_{ss} ($\times 10^{11}$ eV^{-1} cm^{-2})
10	1.100	367.3	0.802	0.188	1.417	0.866	0.761
50	1.180	358.8	1.148	0.187	1.846	1.043	0.601
100	1.145	350.0	1.034	0.187	1.705	0.995	0.634
200	1.152	326.0	1.112	0.187	1.789	1.036	0.702
300	1.132	307.4	1.173	0.188	1.830	1.078	0.719
400	1.069	288.5	1.101	0.189	1.710	1.068	0.823
500	1.002	282.7	0.959	0.191	1.517	1.013	0.944
600	1.469	274.4	1.610	0.181	2.518	1.139	1.158
700	1.384	270.6	1.477	0.183	2.325	1.117	1.260
800	1.346	263.9	1.451	0.183	2.268	1.121	1.332
900	1.327	261.3	1.429	0.184	2.232	1.119	1.404
1000	1.318	266.4	1.462	0.184	2.254	1.137	1.367

C_{ox} represents interface capacitance depending on strong accumulation region and is addressed by the following formula:

$$C_{0x} = C_{ma}\left[1 + \frac{G_{ma}^2}{(\omega C_{ma})^2}\right]. \quad (13)$$

The Nicollian and Brews method is employed to determine the series resistance (R_s) for strong accumulation by the following formula depending on various frequencies[46]:

$$R_s = \frac{G_{ma}}{G_{ma}^2 + (\omega C_{ma})^2}. \quad (14)$$

The calculated N_{ss} and R_s values are tabulated in Table I for frequency ranging from 10 kHz to 1 MHz. The N_{ss} values usually increased via increasing frequency and can follow the ac signal easily. However, the R_s values usually decreased with increasing frequency owing to restructuring and reordering of the interface states by the changing frequency and interfacial $CuCo_2S_4$ layer between the Au metal and *p*-Si.[47,48]

Figure 11 indicates device resistance (R_i) versus voltage graphs of the Au/$CuCo_2S_4$/*p*-Si device for the frequency range of 10 kHz and 1 MHz.R_i values remained constant at the higher inversion region and exhibited peaks at low inversion, accumulation and depletion regions. The inset of Fig. 11 clearly exhibits two different peaks for lower frequencies. The intensity of the peaks decreased with increasing frequency because the interface states cannot follow the ac signal to higher frequencies.[49] The peak behaviors of the R_i values can be attributed to interface state effects.[50]

The capacitance and conductance transient results of the Au/$CuCo_2S_4$/*p*-Si device are demonstrated in Fig. 12a and b, respectively, for increasing light illumination intensities from 20 to 100 mW at 10 kHz frequency. The device clearly exhibited photocapacitance and photoconductance behavior under various light illuminations. The device has

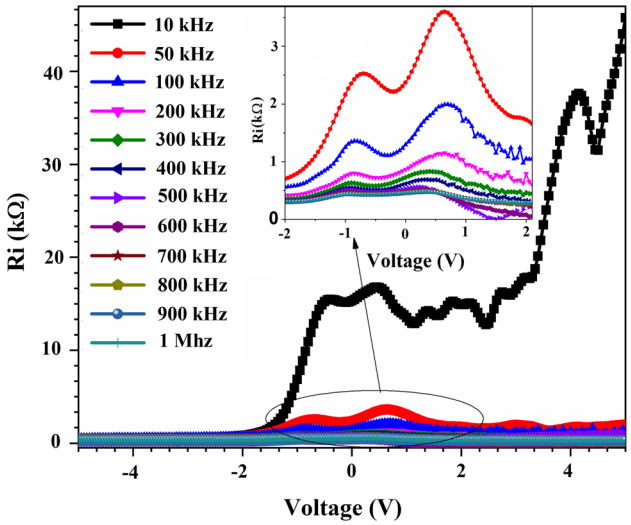

Fig. 11. The resistance–voltage (R_i–V) characteristics of the Au/$CuCo_2S_4$/*p*-Si device.

fast capacitance and conductance response against illumination and can be used in photocapacitor applications due to increasing capacitance depending on the illumination intensity.[51]

CONCLUSION

In summary, in this study, thiospinel $CuCo_2S_4$ nanocrystals were effectively synthesized by a hot-injection synthesis process, and their electrical and optoelectronic properties were studied. The hot-injection method presented in this study showed that thiospinel particles below 10 nm can be obtained in homogeneous atomic distribution. The results obtained in device applications showed that this material can be used in optoelectronic applications. Also, this study will contribute to the detailed elucidation of the thiospinels. The *I*–*V* and *C*–*V* measurements were used to calculate and characterize the electrical and heterojunction parameters and were discussed in detail. The transient photocurrent characteristics of the fabricated devices based on thiospinel particles prove that the devices

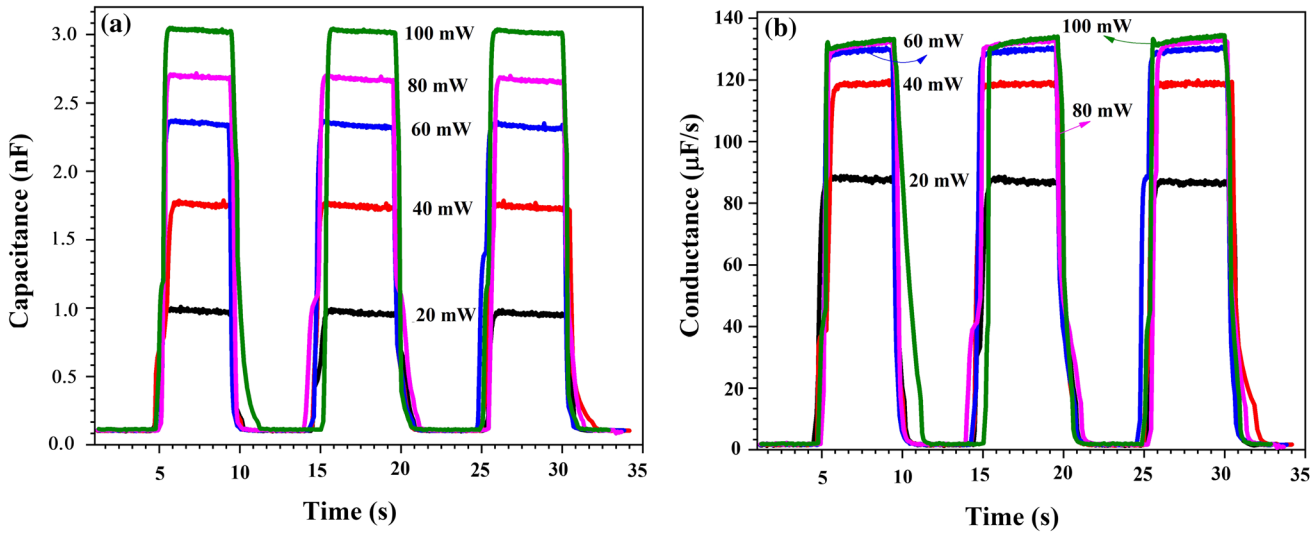

Fig. 12. The capacitance (a) and conductance (b) transient plots of the Au/$CuCo_2S_4$/*p*-Si device for various illumination intensities per cm^2 device area.

show photosensitivity behavior. Moreover, this study will provide a gateway for further investigation of other thiospinel materials and their utility in energy and advancing optoelectronic technologies, especially in photodiode applications.

ACKNOWLEDGMENTS

This work is supported by TUBITAK (The Scientific and Technological Research Council of Turkey) under Project Number 217M212.

REFERENCES

1. A.N. Buckley, W.M. Skinner, S.L. Harmer, A. Pring, and L.J. Fan, *Geochim. Cosmochim. Acta* 73, 4452 (2009).
2. M. Chauhan, K. Soni, P.E. Karthik, K.P. Reddy, C.S. Gopinath, and S. Deka, *J. Mater. Chem. A* 7, 6985 (2019).
3. S. Hariganesh, S. Vadivel, D. Maruthamani, M. Kumaravel, and A. Habibi-Yangjeh, *J. Inorg. Organomet. Polym Mater.* 28, 1276 (2018).
4. Y. Ge, J. Wu, X. Xu, M. Ye, and J. Shen, *Int. J. Hydrogen Energy* 41, 19847 (2016).
5. M. Chauhan, K.P. Reddy, C.S. Gopinath, and S. Deka, *ACS Catal.* 7, 5871 (2017).
6. A.M. Wiltrout, C.G. Read, E.M. Spencer, and R.E. Schaak, *Inorg. Chem.* 55, 221 (2016).
7. X. Du, X. Zhang, Z. Yang, and Y. Gong, *Chem. Asian J.* 13, 266 (2018).
8. L. Chen, Y. Zuo, Y. Zhang, and Y. Gao, *Int. J. Electrochem. Sci.* 13, 1343 (2018).
9. X. Xu, Y. Liu, P. Dong, P.M. Ajayan, J. Shen, and M. Ye, *J. Power Sour.* 400, 96 (2018).
10. S. Cheng, T. Shi, C. Chen, Y. Zhong, Y. Huang, X. Tao, J. Li, G. Liao, and Z. Tang, *Sci. Rep.* 7, 6681 (2017).
11. Q. Li, Q. Jiao, X. Feng, Y. Zhao, H. Li, C. Feng, D. Shi, H. Liu, H. Wang, and X. Bai, *ChemElectroChem* 6, 1558 (2019).
12. B. Li, F. Yuan, G. He, X. Han, X. Wang, J. Qin, Z.X. Guo, X. Lu, Q. Wang, I.P. Parkin, and C. Wu, *Adv. Funct. Mater.* 27, 1606218 (2017).
13. Y. Chen, X. Ji, V. Sethumathavan, and B. Paul, *Materials* 11, 2303 (2018).
14. A. Sarilmaz and F. Ozel, *J. Alloys Compd.* 780, 518 (2019).
15. M. Yıldırım, M.O. Erdal, and A. Kocyigit, *Phys. B* 572, 153 (2019).
16. M.O. Erdal, M. Yıldırım, and A. Kocyigit, *J. Mater. Sci.: Mater. Electron.* 30, 13617 (2019).
17. S. Uruş, M. Çaylar, and İ. Karteri, *Chem. Eng. J.* 306, 961 (2016).
18. F. Özel, A. Sarilmaz, B. Istanbullu, A. Aljabour, M. Kuş, and S. Sönmezoğlu, *Sci. Rep.* 6, 29207 (2016).
19. M. Yıldırım and A. Kocyigit, *J. Alloys Compd.* 768, 1064 (2018).
20. A.S. Dahlan, A. Tataroğlu, A.A. Al-Ghamdi, A.A. Al-Ghamdi, S. Bin-Omran, Y. Al-Turki, F. El-Tantawy, and F. Yakuphanoglu, *J. Alloys Compd.* 646, 1151 (2015).
21. A. Mekki, R.O. Ocaya, A. Dere, A.A. Al-Ghamdi, K. Harrabi, and F. Yakuphanoglu, *Synth. Met.* 213, 47 (2016).
22. S. Kyoung, E.-S. Jung, and M.Y. Sung, *Microelectron. Eng.* 154, 69 (2016).
23. M. Gökçen, T. Tunç, S. Altındal, and I. Uslu, *Curr. Appl. Phys.* 12, 525 (2012).
24. Ş. Aydoğan, M.L. Grilli, M. Yilmaz, Z. Çaldiran, and H. Kaçuş, *J. Alloys Compd.* 708, 55 (2017).
25. Y.-X. Luo and C.-H. Shih, *Semicond. Sci. Technol.* 29, 115006 (2014).
26. İ. Taşçıoğlu, S.O. Tan, F. Yakuphanoğlu, and Ş. Altındal, *J. Electron. Mater.* 47, 6059 (2018).
27. A. Kocyigit, M. Yılmaz, Ş. Aydoğan, and Ü. İncekara, *J. Alloys Compd.* 790, 388 (2019).
28. F. Djeffal, H. Ferhati, A. Benhaya, and A. Bendjerad, *Superlattices Microstruct.* 128, 382 (2019).
29. M.A. Yeganeh, S. Rahmatollahpur, R. Sadighi-Bonabi, and R. Mamedov, *Phys. B* 405, 3253 (2010).
30. S.K. Cheung and N.W. Cheung, *Appl. Phys. Lett.* 49, 85 (1986).
31. M.O. Erdal, A. Kocyigit, and M. Yıldırım, *Mater. Sci. Semicond. Process.* (2019). https://doi.org/10.1016/j.mssp.2019.104620.
32. D.E. Yildiz, Ş. Altindal, and H. Kanbur, *J. Appl. Phys.* 103, 124502 (2008).
33. A.K. Bilgili, T. Güzel, and M. Özer, *J. Appl. Phys.* 125, 035704 (2019).
34. I. Orak, A. Kocyigit, and A. Turut, *J Alloys Compd* 691, 873 (2017).
35. O.S. Cifci, M. Bakir, J.L. Meyer, and A. Kocyigit, *Mater. Sci. Semicond. Process.* 74, 175 (2018).
36. H. Norde, *J. Appl. Phys.* 50, 5052 (1979).
37. B.A. Gozeh, A. Karabulut, A. Yildiz, and F. Yakuphanoglu, *J. Alloys Compd.* 732, 16 (2018).
38. R. Mirzanezhad-Asl, A. Phirouznia, S. Altındal, Y. Badali, and Y. Azizian-Kalandaragh, *Physica B Condens. Matter* 561, 1 (2019).
39. Y. Şafak-Asar, T. Asar, Ş. Altındal, and S. Özçelik, *J Alloys Compd* 628, 442 (2015).

40. D. Korucu, A. Turut, R. Turan, and Ş. Altindal, *Mater. Sci. Semicond. Process.* 16, 344 (2013).
41. R.H. AlOrainy and A.A. Hendi, *Microelectron. Eng.* 127, 14 (2014).
42. E. ErbilenTanrıkulu, Ş. Altındal, and Y. Azizian-Kalandaragh, *J. Mater. Sci.: Mater. Electron.* 29, 11801 (2018).
43. R.H. AlOrainy, *J. Optoelectron. Adv. Mater.* 16, 793 (2014).
44. S.M. Sze, *Physics of Semiconductor Devices*, 2nd ed. (Newyork: Wiley, 1981), pp. 45–46.
45. W.A. Hill and C.C. Coleman, *Solid State Electron.* 23, 987 (1980).
46. E.H. Nicollian and J.R. Brews, *Solid-State Electron.* 27, 953 (1984).
47. S. Zeyrek, E. Acaroğlu, Ş. Altındal, S. Birdoğan, and M.M. Bülbül, *Curr. Appl. Phys.* 13, 1225 (2013).
48. S. Demirezen, Z. Sönmez, U. Aydemir, and Ş. Altındal, *Curr. Appl. Phys.* 12, 266 (2012).
49. I. Orak, A. Kocyigit, and S. Alindal, *Chin. Phys. B* 26, 028102 (2017).
50. N. Baraz, İ. Yücedağ, Y. Azizian-Kalandaragh, and Ş. Altındal, *J. Mater. Sci.: Mater. Electron.* 28, 1315 (2017).
51. A. Mekki, A. Dere, K. Mensah-Darkwa, A. Al-Ghamdi, R.K. Gupta, K. Harrabi, W.A. Farooq, F. El-Tantawy, and F. Yakuphanoglu, *Synth. Met.* 217, 43 (2016).